Petroleum Science 20 (2023) 2127–2140

Contents lists available at ScienceDirect

Petroleum Science

journal homepage: www.keaipublishing.com/en/journals/petroleum-science

Original Paper

Simultaneous denoising and resolution enhancement of seismic data based on elastic convolution dictionary learning

Nan-Ying Lan, Fan-Chang Zhang*, Kai-Heng Sang, Xing-Yao Yin

School of Geosciences, China University of Petroleum (East China), Qingdao, Shandong, 266580, China

ARTICLE INFO

Article history:
Received 17 March 2022
Received in revised form
25 September 2022
Accepted 20 February 2023
Available online 21 February 2023

Edited by Jie Hao

Keywords:
Simultaneous denoising and resolution enhancement
Elastic convolution dictionary learning
Weighted convolutional sparse representation
Matched filtering

ABSTRACT

Enhancing seismic resolution is a key component in seismic data processing, which plays a valuable role in raising the prospecting accuracy of oil reservoirs. However, in noisy situations, existing resolution enhancement methods are difficult to yield satisfactory processing outcomes for reservoir characterization. To solve this problem, we develop a new approach for simultaneous denoising and resolution enhancement of seismic data based on convolution dictionary learning. First, an elastic convolution dictionary learning algorithm is presented to efficiently learn a convolution dictionary with stronger representation capability from the noisy data to be processed. Specifically, the algorithm introduces the elastic $L_{1/2}$ norm as a sparsity constraint and employs a steepest gradient descent strategy to efficiently solve the frequency-domain linear system with substantial computational cost in a half-quadratic splitting framework. Then, based on the learned convolution dictionary, a weighted convolutional sparse representation paradigm is designed to encode the noisy data to acquire an optimal sparse approximation of the effective signal. Subsequently, a high-resolution dictionary with a broadband spectrum is constructed by the proposed parameter scaling strategy and matched filtering technique on the basis of atomic spectrum modeling. Finally, the optimal sparse approximation of the effective signal and the constructed high-resolution dictionary are used for data reconstruction to obtain the seismic signal with high resolution and high signal-to-noise ratio. Synthetic and field dataset examples are executed to check the effectiveness and reliability of the developed method. The results indicate that this method has a more competitive performance in seismic applications compared with the conventional deconvolution and spectral whitening methods.

1. Introduction

With the deepening of exploration and development, the oil and gas industry has shifted its exploration direction from large-scale structural reservoirs to smaller-scale lithologic reservoirs (Kwietniak et al., 2018). Lithologic reservoirs are usually composed of fine-scale geological bodies, such as thin sand beds, sandstone pinchouts, cave-cleft bodies, and lenses, whose accurate identification places a higher demand on the resolution of seismic data. Nevertheless, due to the band-limited property of source wavelet and the energy absorption and spherical diffusion of seismic wave propagation in viscoelastic medium, the collected seismic data have a low resolution that is often insufficient to identify and characterize these small-scale reservoirs (Sheriff and Geldart, 1995; Ikelle and Amundsen, 2005). In addition, side effects of some processing procedures, such as normal moveout correction stretching (Zhang and Lan, 2020) and migration stretching (Perez and Marfurt, 2007), can also reduce the resolution of seismic data. To enhance the certainty of exploration and reduce the development risk of lithologic reservoirs, it is necessary to process these low-resolution seismic data so as to improve their vertical resolution.

Up to now, geophysicists have developed numerous resolution enhancement methods that can be roughly classified into three categories: spectral whitening (Lee, 1986; Rosa and Ulrych, 1991; Manenti and Porsani, 2016; Naghadeh and Morley, 2017), deconvolution (Oldenburg, 1981; Treitel and Lines, 1982; Jin and Eisner, 1984; Margrave et al., 2011; Gholami, 2017; Chen and Wang, 2018; Wang et al., 2020), and inverse Q filtering (Irving and Knight, 2003; Wang, 2006; Yuan et al., 2016; Morozov et al., 2018; Aghamiry and Gholami, 2018; Wang et al., 2018; Shao and Wang, 2021). Spectral

* Corresponding author.
E-mail address: zhangfch@upc.edu.cn (F.-C. Zhang).

https://doi.org/10.1016/j.petsci.2023.02.023

whitening and its variants compensate for the high-frequency components lost in seismic wave propagation by gaining all frequencies in the useful band scope of seismic signal, thereby improving seismic resolution. Typical techniques include frequency-domain spectral whitening (Lee, 1986), time-variant spectral whitening (Naghadeh and Morley, 2017), and spectral blueing (Rosa and Ulrych, 1991; Kazemeini et al., 2010; Kwietniak et al., 2018). This type of method is simple in principle and computationally efficient, so it is most commonly used in practical processing. Unlike spectral whitening and its variants, deconvolution enhances the vertical resolution of seismic data by squeezing the source wavelet and widening the useful frequency band. Oldenburg (1981) first proposed a time-domain deconvolution method based on the least-squares wiener filter. Later, Treitel and Lines (1982) developed a frequency-domain deconvolution algorithm using the linear inversion theory. Both methods have the assumption of stationarity, that is, minimum-phase wavelet and white reflectivity, which greatly limits the practicality of the method. To raise the applicability of this method, several improvements have been presented, such as homomorphic deconvolution (Jin and Eisner, 1984), Gabor deconvolution (Margrave et al., 2011; Gholami, 2016), wavelet scaling-based deconvolution (Chen and Wang, 2018), blind deconvolution (Kazemi and Sacchi, 2014; Sui and Ma, 2020), morphological deconvolution (Gholami, 2017), and adaptive deconvolution (Wang et al., 2020). Besides, inverse Q filtering has been applied to heighten the seismic resolution. Inverse Q filtering, also called absorption compensation, accomplishes its objective by compensating for non-stationary attenuation. Specifically, this method performs amplitude compensation and phase correction for each frequency component according to the theoretical attenuation model based on a proper estimate of the underground Q-values. In the detailed implementation of this method, two different algorithms are proposed: the direct approach (Irving and Knight, 2003; Wang, 2006) and the inversion-based approach (Yuan et al., 2016). The direct approach uses a gain limitation or stabilization factor in the reverse operation of the forward wave propagation to achieve stable attenuation compensation, while the inversion-based approach employs the regularization tool to iteratively minimize the misfit between the synthetic data and the field-collected data to yield optimal desorption outcomes. The three types of resolution enhancement methods mentioned above work well in the applications, but they all share a common premise: the noise contained in the seismic data to be processed is so small that it does not interfere with the high-resolution processing. In fact, the existence of noise is an obstacle that must be overcome to obtain satisfactory enhancement results. Therefore, these above methods always require a separate denoising step prior to their processing.

Different from existing methods, the goal of this paper is to combine the resolution enhancement process with the seismic denoising process and investigate a novel method that can simultaneously attenuate noise and enhance seismic resolution. Convolution dictionary learning (Chun and Fessler, 2018; Song et al., 2020) is a machine learning technology developed in recent years, which can represent seismic signals as a convolution sum of a series of convolution dictionary atoms and their corresponding mapping coefficients. These dictionary atoms adaptively learn the inherent features and can mine detailed information hidden in the seismic signal, providing a promising tool for the implementation of this method. Current convolution dictionary learning is generally defined as an extension of convolutional basis pursuit denoising (Chen et al., 1998), which is essentially a sparse optimization problem with L_1 norm constraints. However, previous work reveals that the L_1 norm can cause a biased issue (Zhang, 2010), leading to unsatisfactory representation results for the learned convolution dictionary (Peng, 2019). Lately, the nonconvex elastic $L_{1/2}$ norm (Lan et al., 2021) has demonstrated significant potential in tackling the biased issue arising from the L_1 norm in numerous inversion works. As an improvement, we introduce the nonconvex elastic $L_{1/2}$ norm into convolution dictionary learning and develop an elastic convolution dictionary learning (ECDL) algorithm to enhance the representation capability of the learned dictionary. Meanwhile, to improve the learning efficiency, we employ a steepest gradient descent strategy to efficiently handle the frequency-domain linear system with a huge computational cost in the half-quadratic splitting framework. Subsequently, based on the developed elastic convolution dictionary algorithm, we propose a novel processing method for simultaneous denoising and resolution enhancement. A series of experiments are performed on synthetic and real datasets to evaluate the performance of this method. Experimental results show the proposed algorithm can effectively broaden the frequency bandwidth and enhance the seismic resolution while greatly attenuating the noise and improving the signal-to-noise ratio (S/N) of the data, which is superior to the conventional deconvolution and spectral whitening approaches.

2. Methodology

2.1. Elastic convolution dictionary learning

Dictionary learning is a flexible framework that can adaptively construct a basis function (dictionary) to achieve the sparse representation of a signal based on the characteristics of the signal itself. Convolution dictionary learning (Chun and Fessler, 2018; Peng, 2019; Song et al., 2020), an important branch of dictionary learning methods, can model the entire signal as the sum of the convolutions between the dictionary atoms and their mapping coefficients. For seismic signals, the introduction of the convolutional form allows the dictionary to preferably capture the structural features of the seismic signal and thus obtain a better representation. Generally, the problem of convolution dictionary learning can be formulated as follows:

$$\underset{\{\mathbf{d}_m\},\{\mathbf{x}_{m,k}\}}{\operatorname{argmin}} \frac{1}{2}\sum_{k=1}^{K}\left\|\mathbf{y}_k-\sum_{m=1}^{M}\mathbf{d}_m * \mathbf{x}_{m,k}\right\|_2^2 + \gamma\sum_{k=1}^{K}\sum_{m=1}^{M}\mathbf{R}(\mathbf{x}_{m,k}) \quad \text{s.t. } \|\mathbf{d}_m\|_2=1,\ \forall m\in\{1,\ldots,M\} \tag{1}$$

where $\mathbf{y}_k$ denotes the k-th training sample, $\mathbf{d}_m$ denotes the m-th dictionary atom, $*$ denotes the convolution operator, $\mathbf{x}_{m,k}$ denotes the mapping coefficients of the training samples $\mathbf{y}_k$ on the dictionary atoms $\mathbf{d}_m$, γ is the regularization parameter, $\mathbf{R}(\cdot)$ represents the prior constraint on the mapping coefficients, notation $\|\cdot\|_2$ denotes the Euclidean norm that aims to avoid scaling ambiguities of dictionary atoms, K and M are the number of dictionary atoms and training samples, respectively. Equation (1) is a typical biconvex optimization problem that is hard to be minimized directly. Fortunately, an indirect means is to minimize it effectively by using iterative strategy and alternating optimization technology. Concretely, each iteration of this algorithm consists of two alternating steps: an encoding step and a dictionary update step. Formulaically, the encoding step and the dictionary update step can be described respectively as

$$\underset{\{\mathbf{x}_{m,k}\}}{\operatorname{argmin}} \frac{1}{2}\sum_{k=1}^{K}\left\|\mathbf{y}_k-\sum_{m=1}^{M}\mathbf{d}_m * \mathbf{x}_{m,k}\right\|_2^2 + \gamma\sum_{k=1}^{K}\sum_{m=1}^{M}\mathbf{R}(\mathbf{x}_{m,k}) \tag{2}$$

$$\underset{\{\mathbf{d}_m\}}{\operatorname{argmin}}\frac{1}{2}\sum_{k=1}^{K}\left\|\mathbf{y}_k-\sum_{m=1}^{M}\mathbf{d}_m{}^{*}\,\mathbf{x}_{m,k}\right\|_2^2\ \text{s.t.}\ \|\mathbf{d}_m\|_2=1 \tag{3}$$

For the encoding step, the conventional algorithm (Zeiler et al., 2010) has focused on the following regularization problems with sparse constraints

$$\underset{\{\mathbf{x}_{m,k}\}}{\operatorname{argmin}}\frac{1}{2}\sum_{k=1}^{K}\left\|\mathbf{y}_k-\sum_{m=1}^{M}\mathbf{d}_m{}^{*}\,\mathbf{x}_{m,k}\right\|_2^2+\gamma\sum_{k=1}^{K}\sum_{m=1}^{M}\left\|\mathbf{x}_{m,k}\right\|_1 \tag{4}$$

where $\|\cdot\|_1$ is the L_1 norm. In fact, Equation (4) is not the optimal constraint form, since the L_1 norm cannot yield an adequately sparse solution (Zhang, 2010; Peng, 2019). In order to gain sufficiently sparse mapping coefficients and thus achieve a lean and compact signal representation, we introduce the most representative sparse constraint format, elastic $L_{1/2}$ norm (Lan et al., 2021), to impose the constraint on the mapping coefficients. Specifically, the encoding step can be expressed as

$$\begin{aligned}&\underset{\{\mathbf{x}_{m,k}\}}{\operatorname{argmin}}\frac{1}{2}\sum_{k=1}^{K}\left\|\mathbf{y}_k-\sum_{m=1}^{M}\mathbf{d}_m{}^{*}\,\mathbf{x}_{m,k}\right\|_2^2\\&+\gamma\sum_{k=1}^{K}\sum_{m=1}^{M}\left(\left\|\mathbf{x}_{m,k}\right\|_{1/2}^{1/2}+\mu\left\|\mathbf{x}_{m,k}\right\|_2^2\right)\end{aligned} \tag{5}$$

where $\|\cdot\|_{1/2}^{1/2}$ denotes the $L_{1/2}$ norm and $\mu\in[0,1]$ is a scalar parameter. To make the solution more convenient, Equation (5) can be equivalently transformed into the following matrix-vector form

$$\underset{\mathbf{X}}{\operatorname{argmin}}\frac{1}{2}\|\mathbf{Y}-\mathbf{D}\mathbf{X}\|_F^2+\gamma\left(\|\mathbf{X}\|_{1/2}^{1/2}+\mu\|\mathbf{X}\|_2^2\right) \tag{6}$$

where $\|\cdot\|_F$ is the Frobenius norm, $\mathbf{Y}=(\mathbf{y}_1\,\mathbf{y}_2\cdots\mathbf{y}_M)$, and $\mathbf{D}=(\mathbf{D}_1\,\mathbf{D}_2\cdots\mathbf{D}_M)$ for which $\mathbf{D}_m$ is defined as $\mathbf{D}_m\mathbf{x}_{m,k}=\mathbf{d}_m{}^{*}\,\mathbf{x}_{m,k}$, and

$$\mathbf{X}=\begin{bmatrix}\mathbf{x}_{1,1}&\mathbf{x}_{1,2}&\cdots&\mathbf{x}_{1,K}\\\mathbf{x}_{2,1}&\mathbf{x}_{2,2}&\cdots&\mathbf{x}_{2,K}\\\vdots&\vdots&\vdots&\vdots\\\mathbf{x}_{M,1}&\mathbf{x}_{M,2}&\cdots&\mathbf{x}_{M,K}\end{bmatrix} \tag{7}$$

By introducing an auxiliary variable $\mathbf{U}=\mathbf{X}$ in Equation (6), we can obtain the equivalent form of this equation

$$\underset{\mathbf{X}}{\operatorname{argmin}}\frac{1}{2}\|\mathbf{Y}-\mathbf{D}\mathbf{X}\|_F^2+\gamma\left(\|\mathbf{U}\|_{1/2}^{1/2}+\mu\|\mathbf{U}\|_2^2\right)\quad\text{s.t.}\ \mathbf{U}=\mathbf{X} \tag{8}$$

Using the half-quadratic splitting (HQS) framework (Mila and Michael, 2005) to solve Equation (8), the following iteration format can be given

$$\mathbf{X}^{(t+1)}=\underset{\mathbf{X}}{\operatorname{argmin}}\frac{1}{2}\|\mathbf{Y}-\mathbf{D}\mathbf{X}\|_F^2+\frac{\lambda}{2}\left\|\mathbf{X}-\mathbf{U}^{(t)}\right\|_F^2 \tag{9a}$$

$$\mathbf{U}^{(t+1)}=\underset{\mathbf{U}}{\operatorname{argmin}}\gamma\left(\|\mathbf{U}\|_{1/2}^{1/2}+\mu\|\mathbf{U}\|_2^2\right)+\frac{\lambda}{2}\left\|\mathbf{X}^{(t+1)}-\mathbf{U}\right\|_F^2 \tag{9b}$$

where t is the number of iterations, λ is the penalty parameter used to control the convergence rate of the algorithm. Equation (9a) is a quadratic optimization problem that has a closed solution

$$\left(\mathbf{D}^T\mathbf{D}+\lambda\mathbf{I}\right)\mathbf{X}^{(t+1)}=\mathbf{D}^T\mathbf{Y}+\lambda\mathbf{U}^{(t)} \tag{10}$$

where $\mathbf{D}^T$ denotes the transpose of the dictionary matrix $\mathbf{D}$, and $\mathbf{I}$ is the identity matrix. In practical applications, it is not practical to solve the linear system shown in Equation (10) directly because it involves the inverse of large matrices. Former research work (Wohlberg, 2014) shows that the efficiency of solving Equation (9a) can be effectively improved with the assistance of the convolution theorem. Transforming Equation (9a) to the frequency domain via the fast Fourier transform (FFT) yields

$$\widehat{\mathbf{X}}^{(t+1)}=\underset{\mathbf{X}}{\operatorname{argmin}}\frac{1}{2}\|\widehat{\mathbf{Y}}-\widehat{\mathbf{D}}\widehat{\mathbf{X}}\|_F^2+\frac{\lambda}{2}\left\|\widehat{\mathbf{X}}-\widehat{\mathbf{U}}^{(t)}\right\|_F^2 \tag{11}$$

where $\widehat{\mathbf{D}}=\mathscr{F}(\mathbf{D})$, $\widehat{\mathbf{X}}^{(t+1)}=\mathscr{F}(\mathbf{X}^{(t)})$, $\widehat{\mathbf{Y}}=\mathscr{F}(\mathbf{Y})$, $\widehat{\mathbf{U}}^{(t)}=\mathscr{F}(\mathbf{U}^{(t)})$, and $\mathscr{F}(\cdot)$ denotes Fourier operator. The solution of the above equation can be given by the following linear system

$$\widehat{\mathbf{X}}^{(t+1)}=\left(\widehat{\mathbf{D}}^H\widehat{\mathbf{D}}+\lambda\mathbf{I}\right)^{-1}\left(\widehat{\mathbf{D}}^H\widehat{\mathbf{Y}}+\lambda\widehat{\mathbf{U}}^{(t)}\right) \tag{12}$$

where the superscript H denotes the conjugate operator of the matrix. Since $\widehat{\mathbf{D}}^H\widehat{\mathbf{D}}$ has a block diagonal structure, the frequency-domain linear system shown in Equation (12) can be decomposed into N (i.e., the length of the signal) independent linear systems. Conventionally, each linear system is solved by the Sherman-Morrison method (Egidi and Maponi, 2006). However, this procedure still has a high computational cost because each linear system needs to perform many iterations during the solving process. To reduce iterations and improve the computational efficiency, we employ a steepest gradient descent strategy to update the coefficient matrix $\widehat{\mathbf{X}}^{(t+1)}$, as

$$\begin{aligned}\widehat{\mathbf{X}}^{(t+1,j+1)}&=\widehat{\mathbf{X}}^{(t+1,j)}-\delta\left(\widehat{\mathbf{D}}^H\left(\widehat{\mathbf{D}}\widehat{\mathbf{X}}^{(t+1,j)}-\widehat{\mathbf{Y}}\right)+\lambda\left(\widehat{\mathbf{X}}^{(t+1,j)}-\widehat{\mathbf{U}}^{(t)}\right)\right)\\&=\overline{\mathbf{B}}\widehat{\mathbf{X}}^{(t+1,j)}+\delta\widehat{\mathbf{D}}^H\widehat{\mathbf{Y}}+\delta\widehat{\mathbf{U}}^{(t)}\end{aligned} \tag{13}$$

where $\overline{\mathbf{B}}=(1-\delta\lambda)\mathbf{I}-\delta\widehat{\mathbf{D}}^H\widehat{\mathbf{D}}$, j is the inner iteration index, and δ is a nonnegative step parameter. Equation (9b) belongs to a typical elastic $L_{1/2}$ norm optimization problem, and it can be easily solved by the elastic half thresholding operation as follows

$$\mathbf{U}^{(t+1)}=\mathscr{H}_{\eta,\xi}\left(\mathbf{X}^{(t+1)}\right) \tag{14a}$$

$$\mathscr{H}_{\eta,\xi}\left(\left[\mathbf{X}^{(t+1)}\right]_{i,l}\right)=\begin{cases}f_{\eta,\xi}\left(\left[\mathbf{X}^{(t+1)}\right]_{i,l}\right),\left|\left[\mathbf{X}^{(t+1)}\right]_{i,l}\right|>\dfrac{3\sqrt[3]{2}}{4}\eta^{2/3}(1+\xi)^{1/3}\\0,\text{otherwise}\end{cases} \tag{14b}$$

$$f_{\eta,\xi}\left(\left[\mathbf{X}^{(t+1)}\right]_{i,l}\right)=\frac{2\left[\mathbf{X}^{(t+1)}\right]_{i,l}}{3(1+\xi)}\left(1+\cos\left(\frac{2\pi}{3}-\frac{2\varphi_{\eta,\xi}\left(\left[\mathbf{X}^{(t+1)}\right]_{i,l}\right)}{3}\right)\right) \tag{14c}$$

$$\varphi_{\eta,\xi}\left(\left[\mathbf{X}^{(t+1)}\right]_{i,l}\right)=\arccos\left(\frac{\eta}{8}(1+\xi)^{1/2}\left(\frac{\left|\left[\mathbf{X}^{(t+1)}\right]_{i,l}\right|}{3}\right)^{-3/2}\right) \tag{14d}$$

where $\eta=\frac{\gamma}{\lambda}$, $\xi=\frac{\gamma\mu}{\lambda}$, $\mathbf{X}^{(t+1)}=\mathscr{F}^{-1}(\widehat{\mathbf{X}}^{(t+1)})$, $\mathscr{F}^{-1}(\cdot)$ represents the inverse Fourier operator, and $[\mathbf{X}^{(t+1)}]_{i,l}$ denotes the element of the i-th row and l-th column of the matrix $\mathbf{X}^{(t+1)}$.

For the dictionary update step, it is actually a convolution version of the constrained optimum direction method (Engan et al., 1999) as follows

$$\underset{\{\mathbf{d}_m\}}{\operatorname{argmin}}\frac{1}{2}\sum_{k=1}^{K}\left\|\mathbf{y}_k-\sum_{m=1}^{M}\mathbf{d}_m*\mathbf{x}_{m,k}\right\|_2^2 \text{ s.t. } \mathbf{d}_m\in G_{PN},\forall m\in\{1,\ldots,M\} \tag{15}$$

where G_{PN} is a set composed of support constraint and normalized constraint, which is defined as

$$G_{PN}=\left\{\mathbf{c}\in\mathbb{R}^N:\left(\mathbf{I}-\mathbf{P}\mathbf{P}^T\right)\mathbf{c}=0,\|\mathbf{c}\|_2=1\right\} \tag{16}$$

where $\mathbf{P}$ represents a zero-padded projection operator. By defining the indicator function of the constraint set as $\iota_{G_{PN}}(S)=\begin{cases}0 & \text{if } S\in G_{PN}\\ \infty & \text{if } S\notin G_{PN}\end{cases}$, Equation (15) can be rewritten into the following unconstrained form

$$\underset{\{\mathbf{d}_m\}}{\operatorname{argmin}}\frac{1}{2}\sum_{k=1}^{K}\left\|\mathbf{y}_k-\sum_{m=1}^{M}\mathbf{d}_m*\mathbf{x}_{m,k}\right\|_2^2+\sum_{m=1}^{M}\iota_{G_{PN}}(\mathbf{d}_m) \tag{17}$$

Defining $\mathbf{Z}_{m,k}\mathbf{d}_m=\mathbf{x}_{m,k}*\mathbf{d}_m$, $\mathbf{d}=(\mathbf{d}_1\,\mathbf{d}_2\cdots\mathbf{d}_M)^T$, $\mathbf{y}=(\mathbf{y}_1\,\mathbf{y}_2\cdots\mathbf{y}_K)^T$ and $\mathbf{Z}=\begin{bmatrix}\mathbf{Z}_{1,1} & \mathbf{Z}_{1,2} & \cdots & \mathbf{Z}_{1,K}\\ \mathbf{Z}_{2,1} & \mathbf{Z}_{2,2} & \cdots & \mathbf{Z}_{2,K}\\ \vdots & \vdots & \vdots & \vdots\\ \mathbf{Z}_{M,1} & \mathbf{Z}_{M,2} & \cdots & \mathbf{Z}_{M,K}\end{bmatrix}$, Equation (17) can be reformulated as

$$\underset{\mathbf{d}}{\operatorname{argmin}}\frac{1}{2}\|\mathbf{y}-\mathbf{Z}\mathbf{d}\|_2^2+\iota_{G_{PN}}(\mathbf{d}) \tag{18}$$

Similar to the encoding step, we also employ the HQS method to solve Equation (18). Introducing the auxiliary variable $\mathbf{g}=\mathbf{d}$ into Equation (18) yields the following constrained optimization problem

$$\underset{\mathbf{d}}{\operatorname{argmin}}\frac{1}{2}\|\mathbf{y}-\mathbf{Z}\mathbf{d}\|_2^2+\iota_{G_{PN}}(\mathbf{g}) \text{ s.t. } \mathbf{d}=\mathbf{g} \tag{19}$$

for which we have the HQS iterations

$$\mathbf{d}^{(i+1)}=\underset{\mathbf{d}}{\operatorname{argmin}}\frac{1}{2}\|\mathbf{y}-\mathbf{Z}\mathbf{d}\|_2^2+\frac{\tau}{2}\left\|\mathbf{d}-\mathbf{g}^{(i)}\right\|_2^2 \tag{20a}$$

$$\mathbf{g}^{(i+1)}=\underset{\mathbf{g}}{\operatorname{argmin}}\iota_{G_{PN}}(\mathbf{g})+\frac{\tau}{2}\left\|\mathbf{d}^{(i+1)}-\mathbf{g}\right\|_2^2 \tag{20b}$$

where τ is a penalty parameter. Analogous to Equation (11), transforming Equation (20a) into the frequency domain using FFT obtains

$$\widehat{\mathbf{d}}^{(i+1)}=\underset{\widehat{\mathbf{d}}}{\operatorname{argmin}}\frac{1}{2}\|\widehat{\mathbf{y}}-\widehat{\mathbf{Z}}\widehat{\mathbf{d}}\|_2^2+\frac{\tau}{2}\left\|\widehat{\mathbf{d}}-\widehat{\mathbf{g}}^{(i)}\right\|_2^2 \tag{21}$$

where $\widehat{\mathbf{d}}=\mathscr{F}(\mathbf{d})$, $\widehat{\mathbf{y}}=\mathscr{F}(\mathbf{y})$, $\widehat{\mathbf{Z}}=\mathscr{F}(\mathbf{Z})$, $\widehat{\mathbf{g}}=\mathscr{F}(\mathbf{g})$. Equation (21) has a closed-form solution that can be given by the following linear system

$$\widehat{\mathbf{d}}=\left(\widehat{\mathbf{Z}}^H\widehat{\mathbf{Z}}+\lambda\mathbf{I}\right)^{-1}\left(\widehat{\mathbf{Z}}^H\widehat{\mathbf{y}}+\tau\widehat{\mathbf{g}}\right) \tag{22}$$

Similarly, we also use the steepest gradient descent strategy to update the main variable $\widehat{\mathbf{d}}$, as

$$\begin{aligned}\widehat{\mathbf{d}}^{(i+1,j+1)}&=\widehat{\mathbf{d}}^{(i+1,j)}-\delta\left(\widehat{\mathbf{Z}}^H\left(\widehat{\mathbf{Z}}\widehat{\mathbf{d}}^{(i+1,j)}-\widehat{\mathbf{y}}\right)+\tau\left(\widehat{\mathbf{d}}^{(i+1,j)}-\widehat{\mathbf{g}}^{(i)}\right)\right)\\&=\overline{\mathbf{A}}\widehat{\mathbf{d}}^{(i+1,j)}+\delta\widehat{\mathbf{Z}}^H\widehat{\mathbf{y}}+\delta\widehat{\mathbf{g}}^{(i)}\end{aligned} \tag{23}$$

where $\overline{\mathbf{A}}=(1-\delta\tau)\mathbf{I}-\delta\widehat{\mathbf{Z}}^H\widehat{\mathbf{Z}}$ and j is the inner iteration index. Equation (20b) is a proximal operator of $\iota_{G_{PN}}(\mathbf{g})$ at the point $\mathbf{d}^{(i+1)}$, and its solution can be calculated by

$$\mathbf{g}^{(i+1)}=\operatorname{prox}_{\iota_{G_{PN}}}\left(\mathbf{d}^{(i+1)}\right)=\frac{\mathbf{P}\mathbf{P}^T\mathbf{d}^{(i+1)}}{\left\|\mathbf{P}\mathbf{P}^T\mathbf{d}^{(i+1)}\right\|_2} \tag{24}$$

where $\operatorname{prox}_{\iota_{G_{PN}}}(\cdot)$ represents the proximal operator, $\mathbf{d}^{(i+1)}=\frac{1}{2}\mathscr{F}^{-1}(\overleftarrow{\mathbf{A}}\,\mathbf{R}(\widehat{\mathbf{d}}^{(i+1)}))+\frac{1}{2}\mathscr{F}^{-1}(\overrightarrow{\mathbf{AR}}(\widehat{\mathbf{d}}^{(i+1)}))$, $\overleftarrow{\mathbf{A}}\,\mathbf{R}(\cdot)$ and $\overrightarrow{\mathbf{AR}}(\cdot)$ denote the forward estimate and backward estimate of the autoregressive operator (Naghizadeh and Sacchi, 2012) that is employed to avoid noise incursion into the atoms. Based on the above description, Algorithm 1 comprehensively summarizes the workflow of the ECDL algorithm developed in this paper.

Algorithm 1. The developed ECDL algorithm summary.

Input: $\{\mathbf{y}_k\}_{k=1}^{K}, \gamma, \mu, \lambda, \tau$;

Initialize variables: $\{\mathbf{d}_m\}_{m=1}^{M}$, $\{\mathbf{x}_{m,k}\}_{k=1}^{K}, \eta = \frac{\gamma}{\lambda}, \xi = \frac{\gamma\mu}{\lambda}$;

Repeat

for t = 1 to T **do**

$\mathbf{D} \leftarrow \mathrm{F}(\mathbf{D}), \mathbf{X}^{(t)} \leftarrow \mathrm{F}\left(\mathbf{X}^{(t)}\right), \mathbf{Y} \leftarrow \mathrm{F}(\mathbf{Y}), \mathbf{U}^{(t)} \leftarrow \mathrm{F}\left(\mathbf{U}^{(t)}\right); \mathbf{X}^{(t+1,1)} \leftarrow \mathbf{X}^{(t)}$;

for j =1 to L **do**

$\mathbf{X}^{(t+1,j+1)} \leftarrow \overline{\mathbf{B}}\mathbf{X}^{(t+1,j)} + \delta\mathbf{D}^{H}\mathbf{Y} + \delta\mathbf{U}^{(t)}$;

$\mathbf{X}^{(t+1)} \leftarrow \mathbf{X}^{(t+1,j+1)}$;

end for

$\mathbf{X}^{(t+1)} \leftarrow \mathrm{F}^{-1}\left(\mathbf{X}^{(t+1)}\right)$; $\mathbf{U}^{(t+1)} \leftarrow \mathrm{H}_{\eta,\xi}\left(\mathbf{X}^{(t+1)}\right)$;

End for

for i = 1 to I **do**

$\mathbf{d}^{(i)} \leftarrow \mathrm{F}\left(\mathbf{d}^{(i)}\right), \mathbf{y} \leftarrow \mathrm{F}(\mathbf{y}), \mathbf{Z} \leftarrow \mathrm{F}(\mathbf{Z}), \mathbf{g}^{(i)} \leftarrow \mathrm{F}\left(\mathbf{g}^{(i)}\right); \mathbf{d}^{(i+1,1)} \leftarrow \mathbf{d}^{(i)}$;

for j=1 to L **do**

$\mathbf{d}^{(i+1,j+1)} \leftarrow \overline{\mathbf{A}}\mathbf{d}^{(i+1,j)} + \delta\mathbf{Z}^{H}\mathbf{y} + \delta\mathbf{g}^{(i)}$;

$\mathbf{d}^{(i+1)} \leftarrow \mathbf{d}^{(i+1,j+1)}$;

end for

$\mathbf{d}^{(i+1)} \leftarrow \frac{1}{2}\mathrm{F}^{-1}\left(\overrightarrow{\mathbf{AR}}\left(\mathbf{d}^{(i+1)}\right)\right) + \frac{1}{2}\mathrm{F}^{-1}\left(\overrightarrow{\mathbf{AR}}\left(\mathbf{d}^{(i+1)}\right)\right); \mathbf{g}^{(i+1)} \leftarrow \frac{\mathbf{P}\mathbf{P}^{T}\mathbf{d}^{(i+1)}}{\left\|\mathbf{P}\mathbf{P}^{T}\mathbf{d}^{(i+1)}\right\|_2}$;

End for

Output: Convolutional dictionary $\{\mathbf{d}_m\}_{m=1}^{M}$ and mapping coefficients $\{\mathbf{x}_{m,k}\}_{k=1}^{K}$.

2.2. Simultaneous denoising and resolution enhancement based on ECDL

In noisy situations, the multichannel seismic signal $\{\mathbf{s}_j\}_{j=1}^{J}$ to be processed can be represented as

$$\mathbf{s}_j = \boldsymbol{u}_j + \mathbf{n}_j,\ \forall j \in \{1, \ldots, J\} \tag{25}$$

where $\boldsymbol{u}_j$ denotes the noise-free signal (also called effective signal), $\mathbf{n}_j$ denotes the random noise, j is the trace index of seismic signal, and J is the total number of seismic traces. Taking the noisy signal to be processed as training samples and learning them with the proposed ECDL algorithm, we can obtain the learned convolution dictionary $\{\mathbf{d}_m\}_{m=1}^{M}$ and the corresponding mapping coefficients $\{\mathbf{x}_{m,j}\}_{j=1}^{J}$ to represent the signal. Since the encoding step in the proposed ECDL algorithm is essentially equivalent to the denoising problem based on convolutional sparse representation (Li et al., 2021), the approximation of the effective signal can be obtained by the following equation

$$\overline{\boldsymbol{u}}_j = \sum_{m=1}^{M} \mathbf{d}_m * \mathbf{x}_{m,j},\ \forall j \in \{1, \ldots, J\} \tag{26}$$

where $\overline{\boldsymbol{u}}_j$ is the approximation of the effective signal.

Unfortunately, the above way does not provide a competitive performance in denoising effect. Thus, a further denoising process is still necessary. Inspired by existing work (Carrera et al., 2019), we design a weighted convolutional sparse representation paradigm to

encode the noisy data to acquire an optimal sparse approximation of the effective signal, which has been shown to greatly boost the performance in subsequent applications. Specifically, the paradigm can be expressed as follows

$$\tilde{\mathbf{x}}_{m,j}=\underset{\{\mathbf{x}_{m,j}\}}{\operatorname{argmin}}\frac{1}{2}\left\|\mathbf{s}_j-\sum_{m=1}^{M}\mathbf{d}_m*\mathbf{x}_{m,j}\right\|_2^2 +\gamma\sum_{m=1}^{M}\left(\left\|\boldsymbol{\omega}_{m,j}\odot\mathbf{x}_{m,j}\right\|_{1/2}^{1/2}+\mu\left\|\boldsymbol{\omega}_{m,j}\odot\mathbf{x}_{m,j}\right\|_2^2\right) \tag{27}$$

where $\tilde{\mathbf{x}}_{m,j}$ is the optimal sparse approximation of the effective signal $\boldsymbol{u}_j$, $\mathbf{s}_j$ is the noisy signal to be processed, the symbol $\odot$ represents the element-wise product, and $\boldsymbol{\omega}_{m,j}$ denotes the weight vector, which is defined as

$$\boldsymbol{\omega}_{m,j}=\frac{\mathbf{1}}{\left(\bar{\mathbf{d}}_m*\bar{\mathbf{u}}_j\right)^2}=\frac{\mathbf{1}}{\left(\mathbf{D}_m^T\bar{\mathbf{u}}_j\right)^2} \tag{28}$$

where $\bar{\mathbf{d}}_m$ is the conjugate filter of dictionary atom $\mathbf{d}_m$, $\mathbf{D}_m$ is the matrix version of the atomic shifts, and $\frac{\mathbf{1}}{(\cdot)}$ denotes point-wise division. The solution procedure of the paradigm shown in Equation (27) is basically the same as the encoding step involved in the developed ECDL algorithm. The only difference is that the auxiliary variable $\mathbf{U}^{(t+1)}$ needs to be updated by the following weighted elastic half thresholding operation:

$$\left[\mathbf{U}^{(t+1)}\right]_{i,j}=\mathscr{H}_{\eta[\mathbf{W}]_{i,j},\xi[\mathbf{W}]_{i,j}}\left(\left[\mathbf{X}^{(t+1)}\right]_{i,j}\right),\forall i\in\{1,\ldots MN\},\forall j\in\{1,\ldots J\} \tag{29a}$$

$$\mathbf{W}=\begin{bmatrix}\boldsymbol{\omega}_{1,1} & \boldsymbol{\omega}_{1,2} & \cdots & \boldsymbol{\omega}_{1,J}\\ \boldsymbol{\omega}_{2,1} & \boldsymbol{\omega}_{2,2} & \cdots & \boldsymbol{\omega}_{2,J}\\ \vdots & \vdots & \vdots & \vdots\\ \boldsymbol{\omega}_{M,1} & \boldsymbol{\omega}_{M,2} & \cdots & \boldsymbol{\omega}_{M,J}\end{bmatrix} \tag{29b}$$

where $\mathbf{W}$ denotes the weight matrix.

While completing the estimation process of the effective signal, we need to construct a new dictionary based on the learned convolution dictionary to enhance the resolution of seismic data. Due to the fact that the seismic resolution is a function of the frequency width of the seismic data (Okaya, 1995), the newly constructed dictionary must have a wider frequency bandwidth than the learned dictionary. For this purpose, we first transform the learned dictionary to the frequency domain and model its amplitude spectrum using the following function

$$W_{\mathbf{d}_m}(f)=c_m|f|^{\zeta_m}\exp\left(-\zeta_m(\alpha_m|f|)^{k_m}\Big/k_m\right),\forall m\in\{1,\ldots M\} \tag{30}$$

where $W_{\mathbf{d}_m}(f)$ is the amplitude spectrum of the atom $\mathbf{d}_m$, f denotes the frequency, c_m and α_m are nonnegative amplitude coefficients, k_m and ζ_m are nonnegative width parameters. For the estimation of the modeling parameters c_m, α_m, k_m, and ζ_m, we do this by solving the following least-squares problem

$$\min_{c_m,\zeta_m,\alpha_m,k_m}\sum_{m=1}^{M}\varepsilon_m^2=\sum_{m=1}^{M}\left\|\ln\left(W_{\mathbf{d}_m}(f)\right)-\ln c_m-\zeta_m\ln|f| -\zeta_m(\alpha_m|f|)^{k_m}\Big/k_m\right\|_2^2 \tag{31}$$

where $\|\cdot\|_2^2$ denotes the square of the L_2 norm, ε_m is the misfit error to be minimized. After we obtain these modeling parameters, the desired spectrum with a wider frequency bandwidth needs to be constructed. In fact, the desired spectrum can be easily constructed by a parameter scaling strategy. To be specific, scaling down both width parameters (i.e., k_m and ζ_m) simultaneously can achieve the above purpose. It should be emphasized that, in practical applications, the scaling of the parameters k_m and ζ_m needs to be optimized by the cross-validation method to make the processing results best fit the geological understanding of the work area. To verify the feasibility of the parameter scaling strategy, a numerical example is provided in Fig. 1. Fig. 1a shows a field seismic trace that is used as a training sample to train the convolution dictionary with optimal representation capability by the ECDL algorithm. Without loss of generality, we randomly select an atom from the learned convolutional dictionary as a validation object. Fig. 1b draws the selected atom. Fig. 1c plots the spectrum (blue solid line) of the atom shown in Fig. 1b and the modeled spectrum (red dotted line) using Equation (30) with the modeling parameters $c_m = 0.0012$, $\alpha_m = 0.0393$, $k_m = 1.833$, and $\zeta_m = 2.785$. From Fig. 1c, we can see that the modeled spectrum is basically consistent with the original spectrum, indicating that the modeling accuracy is satisfactory. By shrinking the parameters k_m and ζ_m ($k_m = 1.633$ and $\zeta_m = 1.385$), we obtain the desired spectrum that is shown in Fig. 1d. As observed in Fig. 1d, the desired spectrum is broadened at both the high and low frequency ends, while the dominant frequency of the atom is also improved. The improvements in bandwidth and dominant frequency clearly show that the proposed parameter scaling strategy effectively enhances the resolution of the dictionary atom.

After obtaining the desired spectrum with a wide frequency bandwidth, the matched filter between the original spectrum and the desired spectrum needs to be estimated according to the least-squares principle. Specifically, assuming that the input of the matched filtering is $W_{\mathbf{d}_m}(f)$ and the desired output is $\widehat{W}_{\mathbf{d}_m}(f)$, the matched filter $H_{\mathbf{d}_m}(f)$ in the least-square sense can be calculated by the following equation

$$H_{\mathbf{d}_m}(f)=\left(\overline{W}_{\mathbf{d}_m}(f)W_{\mathbf{d}_m}(f)+\varsigma^2\right)^{-1}\overline{W}_{\mathbf{d}_m}(f)\widehat{W}_{\mathbf{d}_m}(f),\forall m\in\{1,\ldots,M\} \tag{32}$$

where $\overline{W}_{\mathbf{d}_m}(f)$ is the complex conjugate of $\widehat{W}_{\mathbf{d}_m}(f)$, ς is a small nonnegative factor that is used to ensure the stability of the solution. For different dictionary atoms, the factor ς is usually chosen between 0.001 and 0.01. Once the matched filters are computed by Equation (32), the new high-resolution dictionary can be constructed by applying these filters to the spectrum of the learned atoms through the following equation

$$\widehat{\mathbf{d}}_m=\frac{\mathscr{F}^{-1}\left(\widehat{\mathbf{d}}_m\odot H_{\mathbf{d}_m}(f)\right)}{\left\|\mathscr{F}^{-1}\left(\widehat{\mathbf{d}}_m\odot H_{\mathbf{d}_m}(f)\right)\right\|_2},\forall m\in\{1,\ldots,M\} \tag{33}$$

where $\widehat{\mathbf{d}}_m$ is the new atom with a broadband spectrum. Subsequently, according to Equation (34), the optimal sparse approximation of the effective signal and the constructed high-resolution dictionary are used to reconstruct the seismic traces, which can simultaneously solve the problems of noise elimination and resolution improvement.

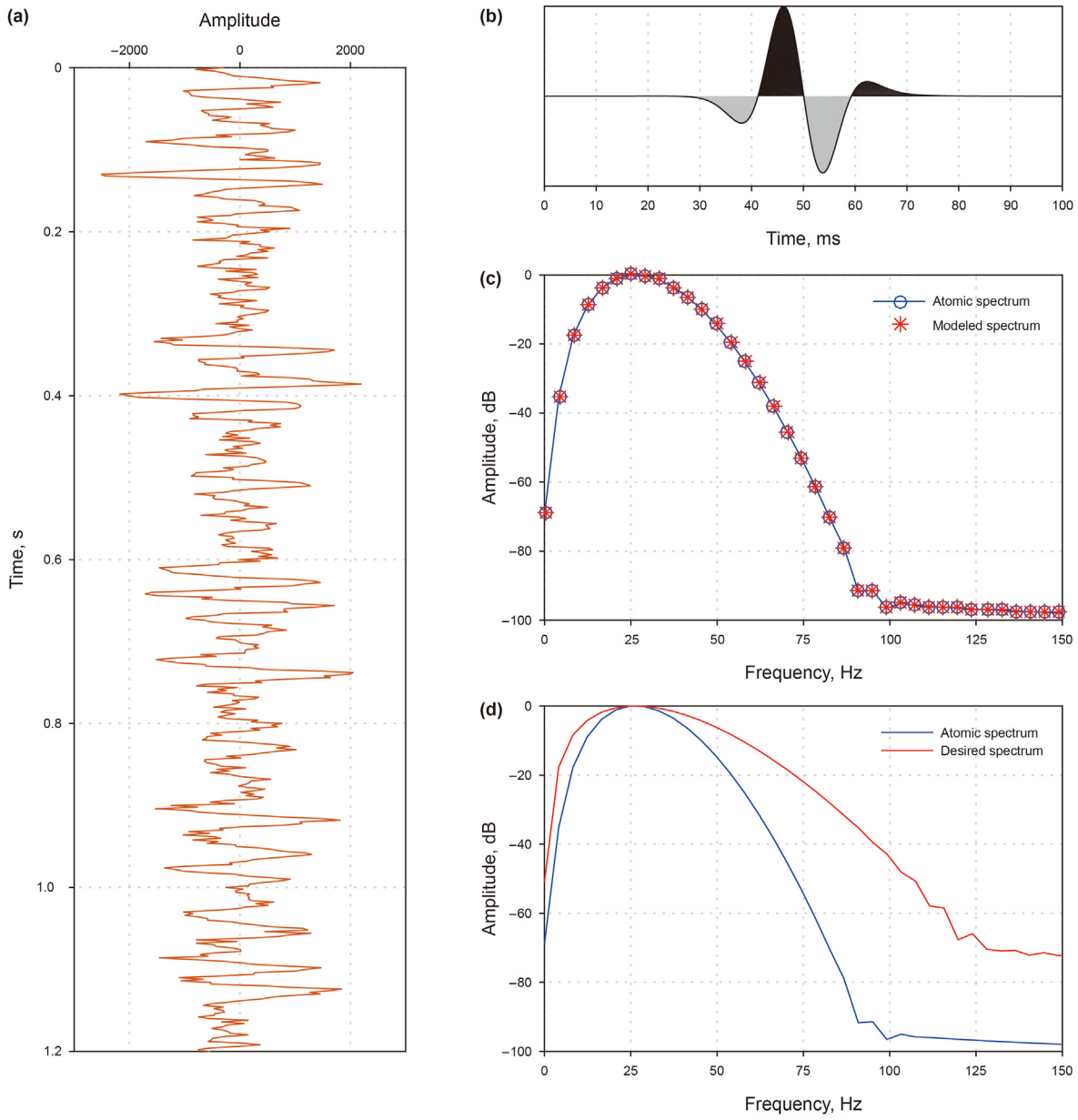

Fig. 1. Efficiency test of the parameter scaling strategy on a field trace. (a) The field seismic trace. (b) An atom learned from (a) using the ECDL algorithm. (c) Modeling of the atomic spectrum. (d) Desired spectrum constructed by the parameter scaling strategy.

$$\widehat{\mathbf{s}}_j = \sum_{m=1}^{M} \widehat{\mathbf{d}}_m * \tilde{\mathbf{x}}_{m,j},\ \forall j \in \{1,\ldots,J\} \tag{34}$$

where $\widehat{\mathbf{s}}_j$ denotes the reconstructed noiseless and high-resolution seismic data. On the basis of the above-mentioned explanation, the detailed working steps of the proposed method can be summarized as follows:

(1) Construct the training sample set using the to-be-processed noisy signal, and learn the convolution dictionary $\{\mathbf{d}_m\}_{m=1}^{M}$ and the corresponding mapping coefficients $\{\mathbf{x}_{m,j}\}_{j=1}^{J}$ from the sample set by employing the ECDL algorithm described in Algorithm 1;

(2) Combine the convolution dictionary and the mapping coefficients by Equation (26) to obtain the initial approximation $\overline{\boldsymbol{u}}_j$ of the effective signal;

(3) Encode the noisy signal according to the weighted convolutional sparse representation paradigm shown in Equation (27) to obtain the optimal sparse approximation $\{\tilde{\mathbf{x}}_{m,j}\}_{j=1}^{J}$ of the effective signal;

(4) Model the atomic spectrum $W_{\mathbf{d}_m}(f)$ by solving Equation (31) and design the desired spectrum $\widehat{W}_{\mathbf{d}_m}(f)$ by scaling the parameters k_m and ζ_m;

(5) Estimate the matched filter $H_{\mathbf{d}_m}(f)$ using Equation (32), and construct the new atom $\widehat{\mathbf{d}}_m$ by applying the matched filter to the frequency spectrum of the dictionary atoms according to Equation (33);

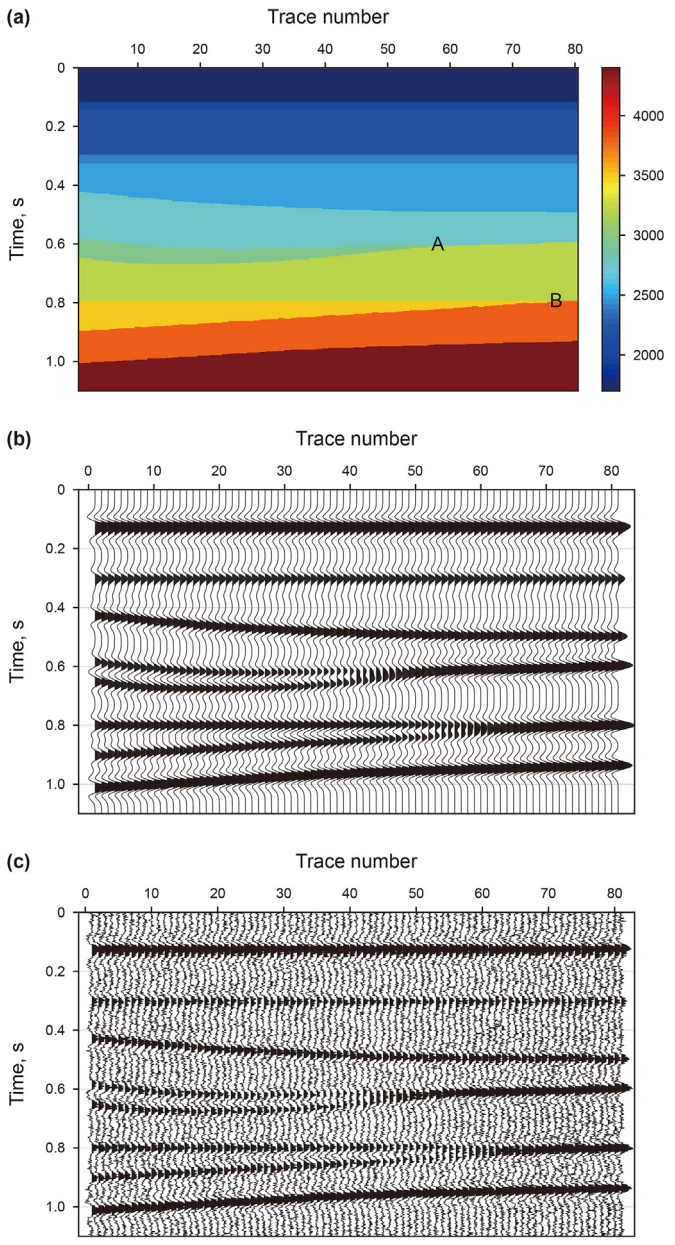

Fig. 2. Synthetic model. (a) Velocity model (unit: m/s). (b) Noise-free synthetic data. (c) Noisy data with 5 dB S/N.

(6) Repeat steps (4)–(5) until all convolution dictionary atoms complete the resolution enhancement procedure;
(7) Reconstruct the noise-free and high-resolution seismic traces $\{\widehat{\mathbf{s}}_j\}_{j=1}^{J}$ using the optimal sparse approximation $\{\tilde{\mathbf{x}}_{m,j}\}_{j=1}^{J}$ of the effective signal and the high-resolution dictionary $\{\widehat{\mathbf{d}}_m\}_{m=1}^{M}$ by Equation (34).

3. Examples

3.1. Synthetic data example

To verify the viability of the proposed method, we use a geological model (Fig. 2a) with known layer thickness and medium properties to create synthetic data. Fig. 2b presents the noise-free synthetic data generated by convolving a 25 Hz Ricker wavelet with the above geological model (tuning thickness = 15.59 ms). In Fig. 2b, the resolution limits of the two thin layers in the shallow part are 26 m and 37 m respectively, which are nowhere near their true thicknesses (13 m and 15 m). Therefore, these two thin layers are indistinguishable in Fig. 2b. The same situation is evident in two wedge-shaped strata of the deep part. To simulate a real noisy situation, we add 5 dB random noise in Fig. 2b and obtain the experimental data shown in Fig. 2c. We use spectral whitening (Naghadeh and Morley, 2017), deconvolution (Treitel and Lines, 1982), and the developed method to process Fig. 2c, and exhibit their results in Fig. 3. Note that the spectral whitening and deconvolution method is not robust in noisy situations, so a denoising process needs to be executed before their processing. In this paper, the denoising step is done by the F-X deconvolution (FX-Decon) method (Gulunay, 1986). As evident in Fig. 3, all three methods effectively resolve two thin layers in the shallow part, indicating that three methods are successful in enhancing seismic resolution. However, the developed method is superior to the other two methods in terms of recognizing thin layers since the events indicated by the red arrows in Fig. 3d are more evident and continuous than those in Fig. 3a and 3b. In addition, we can also find in Fig. 3a and 3b that the deconvolution and spectral whitening methods produce false reflection events and introduce a certain amount of extra interference in the processed result, strengthening the difficulty of accurately identifying valid reflection signals. In contrast, the proposed method better improves the S/N and resolution of seismic data without introducing too much interference (see Fig. 3c).

For a better comparison, Fig. 4a–4d display a local close-up of Fig. 2c and Fig. 3a–3c, respectively. It can be seen from Fig. 4a that, due to resolution limitations, the two reflection events at the top and bottom interfaces of the wedge-shaped strata can only be completely separated at the 42nd trace (onlap termination A) and 57th trace (pinch out termination B) of the synthetic data. After processing by the three methods, the seismic traces that can completely separate the reflection events at the top and bottom interfaces move toward the true locations of terminations A and B, which further demonstrates that all three methods effectively improve the resolution of the data. In addition, we also notice that the deconvolution method and the spectral whitening method can completely separate the top-bottom reflections of two wedge-shaped strata at the 46th and 60th traces, while the method proposed in this paper can separate them at the 47th and 61st traces. This shows that the deconvolution and spectral whitening methods are inferior to the developed method in resolution enhancement. Meanwhile, the above two methods are much worse than the proposed method in terms of fidelity because they introduce more additional interference in the processing results (as marked by the arrows in Fig. 4b and Fig. 4c). To compare the three methods more explicitly, the spectra of Fig. 2 and Fig. 3 are drawn in Fig. 5. Fig. 5a and Fig. 5b plot the spectrum of Fig. 2b and Fig. 2c, respectively. Fig. 5c plots the spectrum of Fig. 3a and clearly shows that the deconvolution method effectively broadens the bandwidth of the synthetic data, but it also retains visible noise. Fig. 5d shows the spectrum of Fig. 3b. It can be evidently viewed that the noise is greatly suppressed and the bandwidth of the data is significantly expanded after processing by the spectral whitening method. Fig. 5e shows the spectrum of Fig. 3c. From Fig. 5e, we can find that the developed method obtains a cleaner and wider spectrum than the other two methods. This result indicates that the method proposed in this paper works more effectively and satisfactorily in terms of simultaneous denoising and resolution improvement.

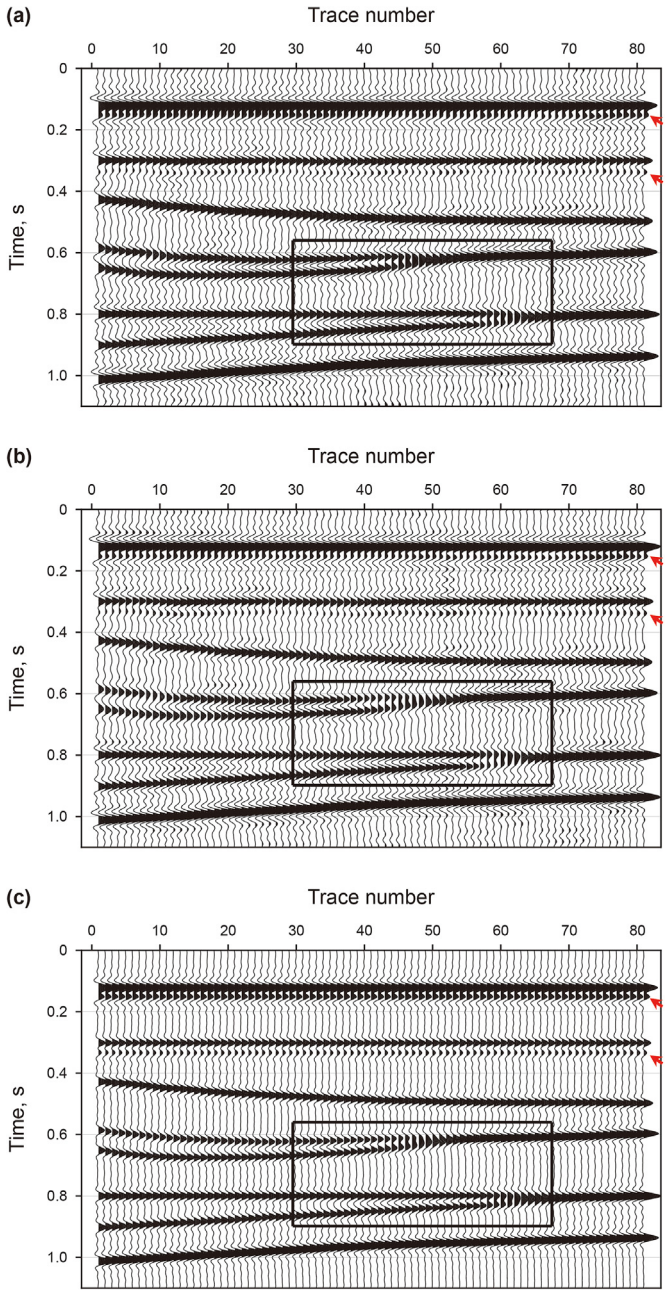

Fig. 3. Comparison of the results of different methods on synthetic data. (a) The result obtained by the deconvolution method. (b) The result obtained by the spectral whitening method. (c) The result obtained by the proposed method. Note that deconvolution and spectral whitening methods need to be preprocessed by the FX-Decon method to eliminate noise interference, which is not required for the proposed method. The events shown by the red arrows in (c) are more obvious and continuous than those in (a) and (b), meaning that the proposed method outperforms the other two methods in resolving thin layers. In addition, as indicated by the black rectangle, (c) is cleaner than (a) and (b), which indicates that the processing result of the proposed method has a higher S/N.

3.2. Field data example

To evaluate the effectiveness of the proposed method in practical processing, we apply it to a field post-stack profile. Fig. 6a shows the profile that consists of 478 traces with 501 sampling points and a sampling interval of 1 ms. In Fig. 6a, the reservoir is located between 1.2 s and 1.4 s. Due to the influence of overlying high-velocity bodies and noise, this post-stack profile has a low signal-to-noise ratio and resolution, causing more difficulty in identifying and tracking the reservoir reflection events. To effectively tackle this issue, we use deconvolution, spectral whitening, and the proposed method to process it. Like the synthetic example, this profile needs to be preprocessed with the FX-Decon method to attenuate noise and highlight the effective signal before using deconvolution and spectral whitening methods. Fig. 6b–6d draw the results of deconvolution, spectral whitening, and the proposed method, respectively. It is clear from Fig. 6 that the noise is greatly eliminated and the seismic resolution is significantly enhanced after processing by the three methods. Further analysis of Fig. 6 reveals that the proposed method is better than the deconvolution and spectral whitening approaches in terms of processing effect because the section obtained by this method has better lateral continuity and higher resolution. To make the comparison more obvious, we enlarge the rectangular area of each subplot in Fig. 6 and show them in Fig. 7. Fig. 7a shows the local enlargement of the original data (Fig. 6a). From Fig. 7a, we can see that the noise destroys the continuity of seismic reflection as well as masks the fault information, which seriously affects the subsequent reservoir prediction work. Fig. 7b shows the local enlargement of the result obtained by the deconvolution method. We can observe that although the deconvolution method improves the seismic resolution and reveals the hidden features to some extent, there are obvious artifacts (between traces 300 and 350) in the processed profile. Fig. 7c and 7d show the local enlargement of the result obtained by the spectral whitening method and the proposed method, respectively. As seen in Fig. 7c and 7d, both methods greatly enhance the resolution of the thin sand layer. The originally discontinuous and weak thin reflection events become continuous and strong reflection events (as shown by arrows), which is meaningful for improving reservoir prediction accuracy. Comparing Fig. 7c and Fig. 7d, it can be found that the processing result of the presented method has higher resolution and better event continuity than that of the spectral whitening method. Additionally, we can also observe from Fig. 7 that the proposed method outperforms the spectral whitening and deconvolution methods in highlighting and portraying hidden features (especially fault system), as indicated in the red rectangles.

In order to further compare and analyze the processing effect of the three methods, we portray the spectra of Fig. 6 in Fig. 8. Although the deconvolution method significantly widens the frequency bandwidth (see Fig. 8b), it does not sufficiently enhance the high-frequency components. This is the reason why the deconvolution method has a lower resolution than the other two methods. From Fig. 8c, we can see that the spectral whitening method can expand the amplitude spectrum to fit the required bandwidth, but it also suppresses some low-frequency components of the effective signal. In contrast, the presented method effectively broadens the bandwidth of seismic data while preserving low-frequency information and boosting the dominant frequency of the data, as shown in Fig. 8d. To check the rationality of the processing results, Fig. 9 shows the well-to-seismic calibration diagrams before and after the processing by the three methods. Fig. 9a shows the well-to-seismic calibration diagram before processing, in which the red curve is the synthetic seismogram created by well logging and Ricker wavelet, the blue curve is the through-well trace, and the black curves are the traces next to the borehole. As visible in Fig. 9a, the original data has low resolution and S/N, so the matching degree between the through-well trace and the synthetic seismogram is poor (shown by the green arrows). Fig. 9b–9d show the well-to-

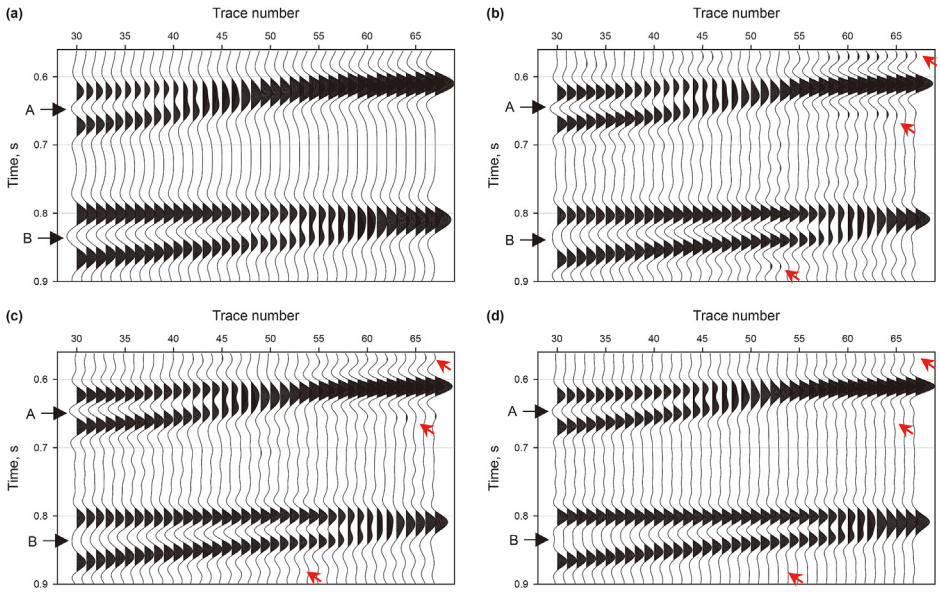

Fig. 4. Local close-up comparison of the synthetic data example. (a) Local close-up of the noise-free synthetic data. (b) Local close-up of the result obtained by deconvolution. (c) Local close-up of the result obtained by spectral whitening. (d) Local close-up of the result obtained by the proposed method. Note that (d) can better identify both termination A and B compared to (b) and (c), implying that the proposed method has a higher resolution. Meanwhile, as shown by the red arrows, more false reflection events are produced in (b) and (c) compared to (d), which means that the method proposed in this paper is superior to the other two methods in terms of fidelity.

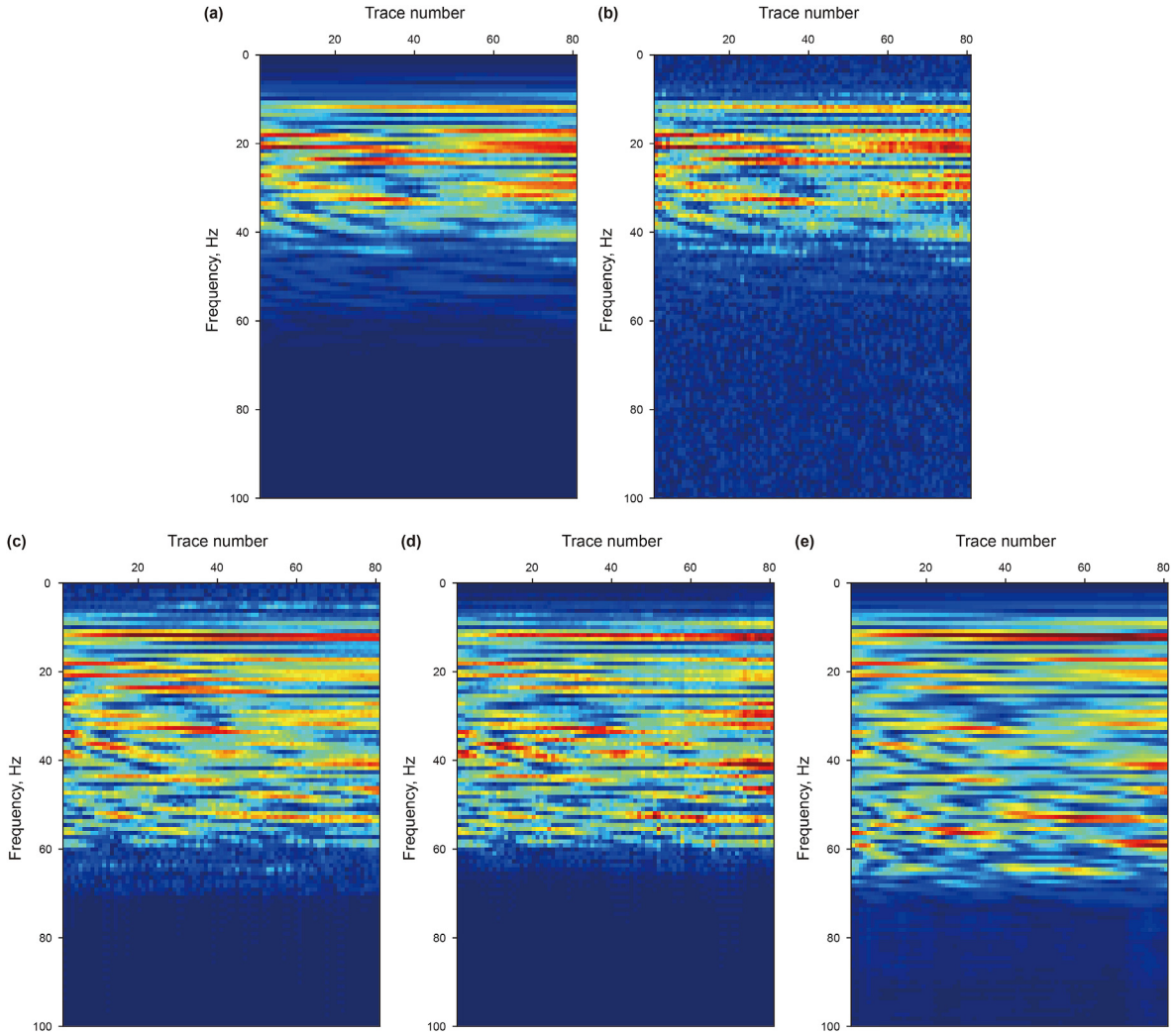

Fig. 5. Spectra comparison of the synthetic data example. (a) The spectrum of the noise-free synthetic data. (b) The spectrum of the noisy synthetic data. (c) The spectrum of the result obtained by deconvolution. (d) The spectrum of the result obtained by spectral whitening. (e) The spectrum of the result obtained by the proposed method.

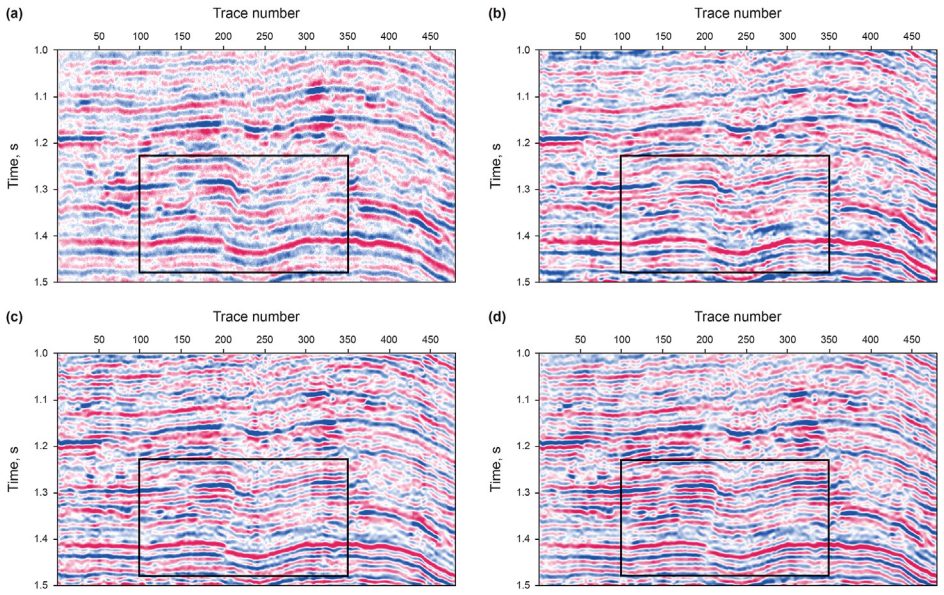

Fig. 6. Field post-stack data example. (a) Noisy field post-stack data. (b) The result of the deconvolution method. (b) The result of the spectral whitening method. (c) The result of the proposed method. Note that deconvolution and spectral whitening methods need to be preprocessed by the FX-Decon method to eliminate noise interference, while the proposed method does not. As the black rectangles indicates, the section obtained by the proposed method has better lateral continuity and higher resolution than those obtained by the other two methods.

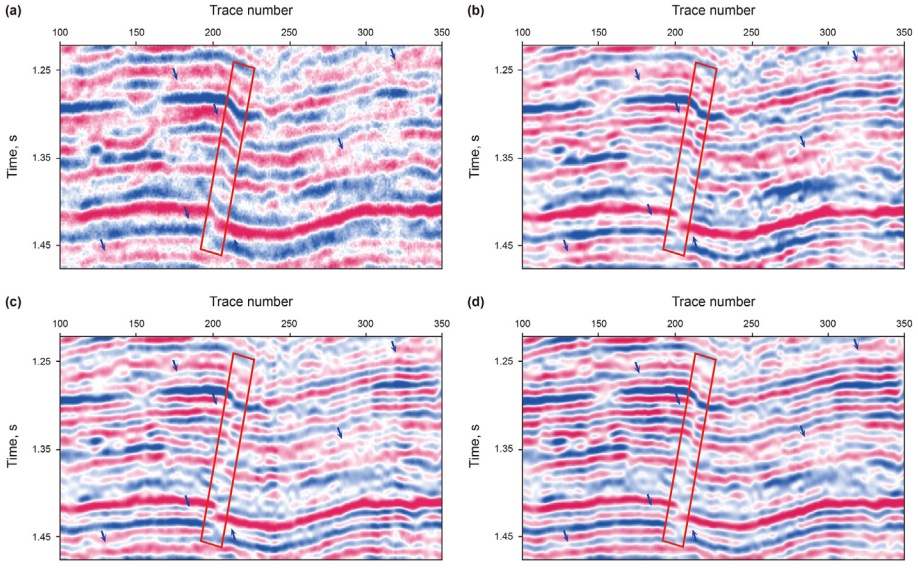

Fig. 7. Zoomed comparison of the field post-stack data example. (a) Noisy field post-stack data. (b) The result of the deconvolution method. (c) The result of the spectral whitening method. (d) The result of the proposed method. Note that as indicated by the blue arrows, the events in (b) and (c) have inferior continuity, while they have good continuity in (d). Also, as shown in the red rectangles, the fault features are better highlighted and characterized in (d) compared to (b) and (c).

seismic calibration diagrams processed by deconvolution, spectral whitening, and the proposed method, respectively. It can be seen from Fig. 9b–9d that after processing by the three methods, the resolution and S/N of the seismic data are markedly boosted, and the matching degree between the through-well trace and the synthetic trace is greatly enhanced. As far as the resolution enhancement effect is concerned, our proposed method works best because the thin layers indicated by the red arrows can be distinguished in Fig. 9d while they cannot well be identified in Fig. 9b and Fig. 9c. For quantitative comparison, we compute the correlation coefficient between the synthetic seismogram and the through-well trace in Fig. 9. The correlation coefficients of Fig. 9a–9d are 0.3571, 0.5948, 0.6107 and 0.7351, respectively. This clearly illustrates that the method proposed in this paper is also superior to the other two methods in terms of the reliability of the processing result. In summary, the proposed method is a reliable technology that can simultaneously improve the resolution and S/N of seismic data, and has promising applications in lithologic reservoir identification and characterization.

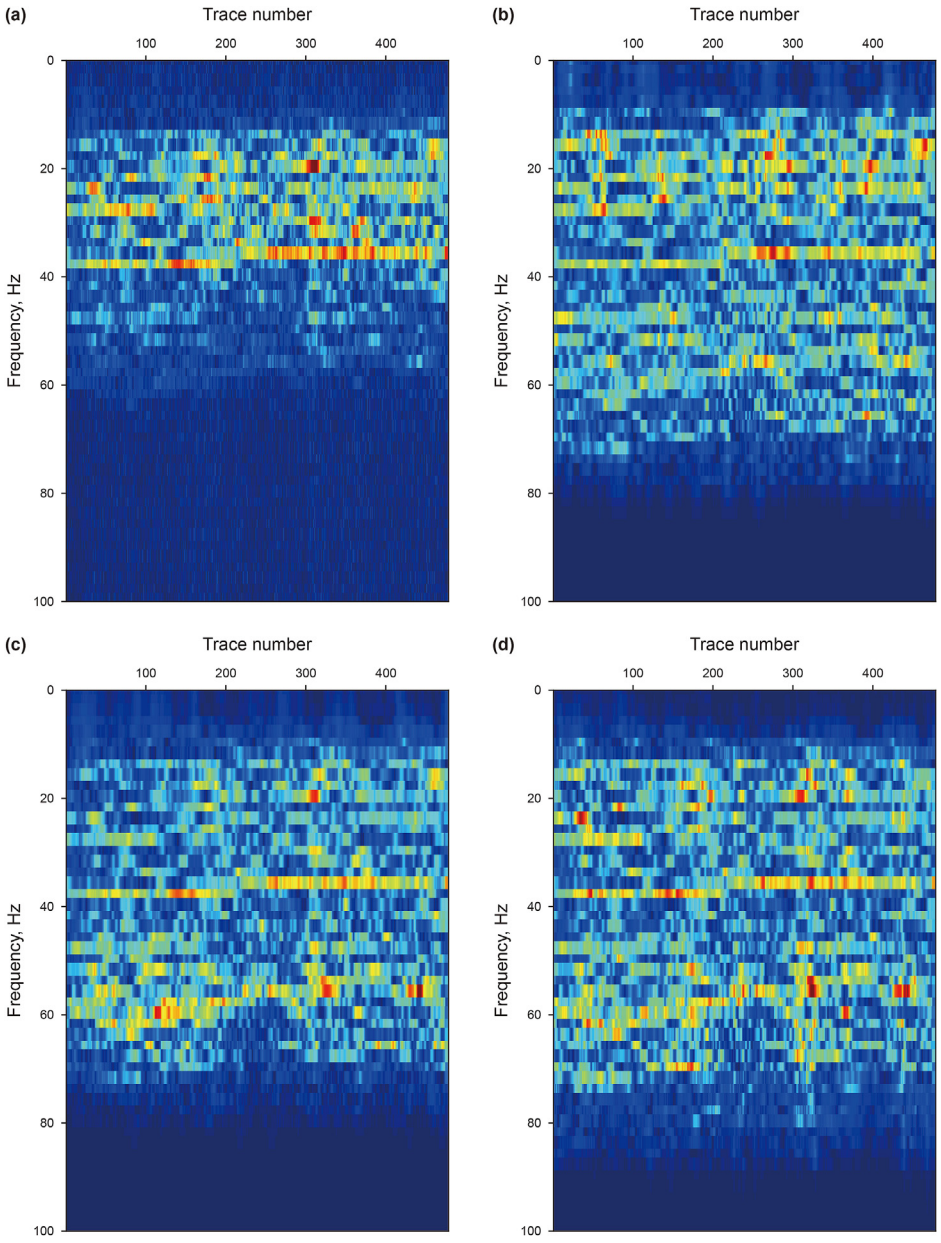

Fig. 8. Spectra comparison of the field post-stack data example. (a) The spectrum of the noisy field post-stack data. (b) The spectrum of the result obtained by deconvolution. (c) The spectrum of the result obtained by spectral whitening. (d) The spectrum of the result obtained by the proposed method.

4. Conclusions

In this paper, we propose a novel processing method for simultaneous denoising and resolution enhancement of seismic data. Specifically, this method employs the elastic convolution dictionary learning developed in this paper as a theoretical framework to solve the problem that the resolution enhancement effect is restricted by noise. To this end, we first develop a weighted convolutional sparse representation paradigm to encode the noisy data to obtain the optimal approximation of the effective signal in the dictionary domain. To enhance the seismic resolution, we then propose a new approach for constructing the high-resolution convolution dictionary, whose steps include modeling the spectra of the learned dictionary atoms, designing the desired spectra for the atoms with a parameter scaling strategy, and broadening the atomic spectrum using matched filtering technology. By adding up the convolution result between the optimal sparse approximation of the effective signal and the constructed high-resolution dictionary, we finally reconstruct the seismic data with both high resolution and high S/N. We use a synthetic record and a field seismic section to examine the accuracy of the proposed method. Our results demonstrate that, in comparison to the conventional deconvolution and spectral whitening methods, the proposed method is more competitive in seismic applications and can provide reliable supporting data for fine exploration and development of oil reservoirs.

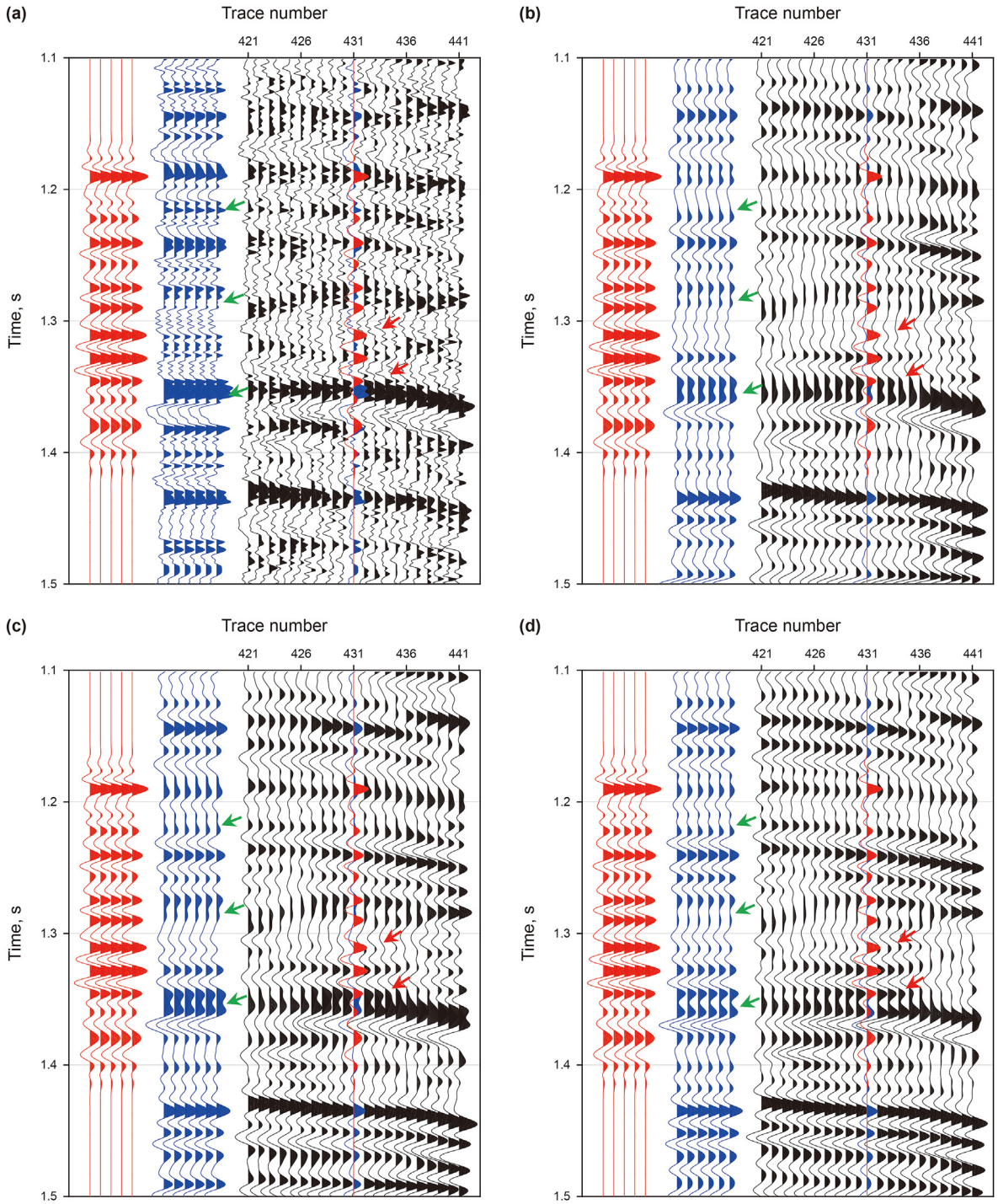

Fig. 9. Comparison of well-to-seismic calibration of field data example. (a) Well-to-seismic calibration of the original field data. (b) Well-to-seismic calibration of the result obtained by deconvolution. (c) Well-to-seismic calibration of the result obtained by spectral whitening. (d) Well-to-seismic calibration of the result obtained by the proposed method. Notice that, as shown by the green arrows, the through-well traces in (b) and (c) are poorly matched with the well synthetic seismogram, but the through-well trace in (d) adequately ties with the synthetic seismogram. At the same time, the thin layers indicated by the red arrows can be distinguished in (d) while they cannot well be identified in (b) and (c). They all demonstrate that the proposed method works best.

Acknowledgments

We are grateful to all the reviewers for their helpful comments on this paper. This work is supported by the Laoshan National Laboratory of Science and Technology Foundation (No. LSKJ202203400) and the National Natural Science Foundation of China (No. 41874146).

References

Aghamiry, H.S., Gholami, A., 2018. Interval-Q estimation and compensation: an adaptive dictionary-learning approach. Geophysics 83 (4), V233–V242. https://doi.org/10.1190/geo2017-0001.1.

Carrera, D., Foi, A., Boracchi, G., et al., 2019. On the weighting for convolutional sparse coding. In: Signal Processing with Adaptive Sparse Structured Representations (SPARS) Workshop.

Chen, S., Donoho, D.L., Saunders, M.A., 1998. Atomic decomposition by basis pursuit. SIAM J. Sci. Comput. 20 (1), 33–61. https://doi.org/10.1137/S003614450037906X.
Chen, S., Wang, Y., 2018. Seismic resolution enhancement by frequency-dependent wavelet scaling. IEEE.Geosci. Rem. Sens. Lett. 15 (5), 654–658. https://doi.org/10.1109/LGRS.2018.2809564.
Chun, Y., Fessler, J.A., 2018. Convolutional dictionary learning: acceleration and convergence. IEEE Trans. Image Process. 27 (4), 1697–1712. https://doi.org/10.1109/TIP.2017.2761545.
Egidi, N., Maponi, P., 2006. A Sherman–Morrison approach to the solution of linear systems. J. Comput. Appl. Math. 189 (2), 703–718. https://doi.org/10.1016/j.cam.2005.02.013.
Engan, K., Aase, S.O., Husøy, J.H., 1999. Method of optimal directions for frame design. In: IEEE International Conference on Acoustics, Speech and Signal Processing, pp. 2443–2446. https://doi.org/10.1109/icassp.1999.760624, 5.
Gholami, A., 2016. Projected gabor deconvolution. Geophysics 81 (2), V151–V157. https://doi.org/10.1190/GEO2015-0412.1.
Gholami, A., 2017. Morphological deconvolution. Geophysics 82 (5), V311–V320. https://doi.org/10.1190/GEO2016-0666.1.
Gulunay, N., 1986. FXDECON and Complex Wiener Prediction Filter. SEG Technical Program Expanded Abstracts, pp. 279–281. https://doi.org/10.1190/1.1893128.
Ikelle, L.T., Amundsen, L., 2005. Introduction to Petroleum Seismology. SEG.
Irving, J.D., Knight, R.J., 2003. Removal of wavelet dispersion from ground-penetrating radar data. Geophysics 68 (3), 960–970. https://doi.org/10.1190/1.1581068.
Jin, D.J., Eisner, E., 1984. A review of homomorphic deconvolution. Rev. Geophys. 22 (3), 255–263. https://doi.org/10.1029/RG022i003p00255.
Kazemeini, S.H., Yang, C., Juhlin, C., et al., 2010. Enhancing seismic data resolution using the prestack blueing technique: an example from the Ketzin CO2 injection site, Germany. Geophysics 75 (6), V101–V110. https://doi.org/10.1190/1.3483900.
Kazemi, N., Sacchi, M.D., 2014. Sparse multichannel blind deconvolution. Geophysics 79 (5), V143–V152. https://doi.org/10.1190/geo2013-0465.1.
Kwietniak, A., Cichostępski, K., Pietsch, K., 2018. Resolution enhancement with relative amplitude preservation for unconventional targets. Interpretation 6 (3), SH59–SH71. https://doi.org/10.1190/INT-2017-0196.1.
Lan, N.Y., Zhang, F.C., Li, C.H., 2021. Robust high-dimensional seismic data interpolation based on elastic half norm regularization and tensor dictionary learning. Geophysics 86 (5), V431–V444. https://doi.org/10.1190/geo2020-0784.1.
Lee, M.W., 1986. Spectral whitening in the frequency domain. US Geological Survey 86–108.
Li, G., He, Z., Tang, J., et al., 2021. Dictionary learning and shift-invariant sparse coding denoising for controlled-source electromagnetic data combined with complementary ensemble empirical mode decomposition. Geophysics 86 (3), E185–E198. https://doi.org/10.1190/geo2020-0246.1.
Manenti, R., Porsani, M., 2016. Spectral Whitening Using Single-Trace Singular Value Decomposition Applied to Vibroseis Data. SEG Technical Program Expanded Abstracts, pp. 4825–4829. https://doi.org/10.1190/segam2016-13960140.1.
Margrave, G.F., Lamoureux, M.P., Henley, D.C., 2011. Gabor deconvolution: estimating reflectivity by nonstationary deconvolution of seismic data. Geophysics 76 (3), W15–W30. https://doi.org/10.1190/1.3560167.
Mila, N., Michael, K.N., 2005. Analysis of half-quadratic minimization methods for signal and image recovery. SIAM J. Sci. Comput. 27 (3), 937–966. https://doi.org/10.1137/030600862.
Morozov, I., Haiba, M., Deng, W., 2018. Inverse attenuation filtering. Geophysics 83 (2), V135–V147. https://doi.org/10.1190/geo2016-0211.1.
Naghadeh, D.H., Morley, C.K., 2017. Enhancement of temporal resolution using improved time-variant spectral whitening. J. Geophys. Eng. 14 (4), 822–832. https://doi.org/10.1088/1742-2140/aa6ddf.
Naghizadeh, M., Sacchi, M., 2012. Multicomponent f-x seismic random noise attenuation via vector autoregressive operators. Geophysics 77 (2), V91–V99. https://doi.org/10.1190/GEO2011-0198.1.
Okaya, D.A., 1995. Spectral properties of the earth's contribution to seismic resolution. Geophysics 60 (1), 241–251. https://doi.org/10.1190/1.1443752.
Oldenburg, D.W., 1981. A comprehensive solution to the linear deconvolution problem. Geophys. J. Int. 65 (2), 331–357. https://doi.org/10.1111/j.1365-246x.1981.tb02716.x.
Peng, G.J., 2019. Adaptive ADMM for dictionary learning in convolutional sparse representation. IEEE Trans. Image Process. 28 (7), 3408–3422. https://doi.org/10.1109/TIP.2019.2896541.
Perez, G., Marfurt, K.J., 2007. Improving lateral and vertical resolution of seismic images by correcting for wavelet stretch in common-angle migration. Geophysics 72 (6), C95–C104. https://doi.org/10.1190/1.2781619.
Rosa, A.L.R., Ulrych, T.J., 1991. Processing via spectral modeling. Geophysics 56 (8), 1244–1251. https://doi.org/10.1190/1.1443144.
Sheriff, R.E., Geldart, L.P., 1995. Exploration Seismology. Cambridge University Press.
Shao, J., Wang, Y.B., 2021. Simultaneous inversion of Q and reflectivity using dictionary learning. Geophysics 86 (5), R763–R776. https://doi.org/10.1190/geo2020-0095.1.
Song, A.H., Flores, F.J., Ba, D., 2020. Convolutional dictionary learning with grid refinement. IEEE Trans. Signal Process. 68, 2558–2573. https://doi.org/10.1109/TSP.2020.2986897.
Sui, Y., Ma, J., 2020. Blind sparse-spike deconvolution with thin layers and structure. Geophysics 85 (6), V481–V496. https://doi.org/10.1190/geo2019-0423.1.
Treitel, S., Lines, L.R., 1982. Linear inverse theory and deconvolution. Geophysics 47 (8), 1153–1159. https://doi.org/10.1190/1.1441378.
Wang, L., Zhou, H., Wang, Y., et al., 2020. Adaptive seismic single-channel deconvolution via convolutional sparse coding model. IEEE.Geosci. Rem. Sens. Lett. 17 (8), 1415–1419. https://doi.org/10.1109/LGRS.2019.2945799.
Wang, Y., 2006. Inverse Q-filter for seismic resolution enhancement. Geophysics 71 (3), V51–V60. https://doi.org/10.1190/1.2192912.
Wang, Y.F., Ma, X., Zhou, H., et al., 2018. L1–2 minimization for exact and stable seismic attenuation compensation. Geophys. J. Int. 213 (3), 1629–1646. https://doi.org/10.1093/gji/ggy064.
Wohlberg, B., 2014. Efficient convolutional sparse coding. In: IEEE International Conference on Acoustics, Speech and Signal Processing, pp. 7173–7177. https://doi.org/10.1109/icassp.2014.6854992.
Yuan, S., Wang, S., Tian, N., et al., 2016. Stable inversion-based multitrace deabsorption method for spatial continuity preservation and weak signal compensation. Geophysics 81 (3), V199–V212. https://doi.org/10.1190/geo2015-0247.1.
Zhang, F.C., Lan, N.Y., 2020. Seismic-gather wavelet-stretching correction based on multiwavelet decomposition algorithm. Geophysics 85 (5), V377–V384. https://doi.org/10.1190/geo2018-0835.1.
Zhang, T., 2010. Analysis of multi-stage convex relaxation for sparse regularization. J. Mach. Learn. Res. 11, 1081–1107.
Zeiler, M.D., Krishnan, D., Taylor, G.W., et al., 2010. Deconvolutional networks. In: IEEE Conference on Computer Vision and Pattern Recognition, pp. 2528–2535. https://doi.org/10.1109/CVPR.2010.5539957.